CHAPTER 1

Introduction and Methods

With the renewed interest over the past decade in problems concerning atomic-scale structure due to the nanotechnology revolution, transmission electron microscopy (TEM) has become an increasingly important materials characterization tool. Its strengths lie in its inherent versatility combined with relatively small size and cost, and widespread availability. The standard operating mode in the electron microscope is direct imaging, widely used in morphological studies, defect studies, and certain types of atomic scale investigations. By changing lens excitations in the imaging system, the diffraction pattern of the illuminated region is displayed, providing detailed structure and symmetry information with excellent signal to noise ratio.

Attachments are available to augment the spatial information with chemical information through the use of X-ray detectors and electron energy loss spectrometers (EELS), and equipment is also available for specialized studies, for example *in-situ* attachments for studying environmental reactions, electron holography for investigating magnetic materials, and through-focal series reconstruction and tomography which yield structure information to high spatial resolution (Spence 2003). The simultaneous availability of different types of information has made EM very important in many areas of chemistry, biology, and materials science. Elucidation of several important structures such as carbon nanotubes, several superconducting materials, quasicrystals, and many proteins were possible because of the instrument's inherent versatility. As the length scale of materials problems steadily decreases, atomic-scale structural electron crystallography will be seeing more demand.

Catalysis is a particularly important area of application. Refinement of hydrocarbons is a multi-billion dollar industry that ranges from the initial processing of crude oil to the green catalysis of spent fuels. Not only does structural knowledge enable detailed understanding of reaction characteristics, it opens the door for improvement of catalytic mechanisms at the atomic scale, and later facilitates industrial protection of new catalyst structures by way of patents. The latter is a very strong incentive to shift structure studies from large shared facilities into the industrial laboratory, where characterization can occur rapidly and behind closed doors, and ideally at reduced cost.

This Ph.D. thesis concerns the implementation and development of precession electron diffraction (PED), a modification of the transmission electron diffraction mode (TED) intended for atomic-scale characterization of bulk materials. PED has demonstrated great promise for overcoming significant data quality limitations and represents a major step toward the realization of rapid atomic structure characterization in the TEM. This work is divided into two

parts: 1) general implementation of a high-performance precession system, and 2) application of the PED system to model materials systems for the purpose of understanding the technique's limitations and to refine its capabilities. Three practical precession systems are provided in the appendices to provide a guide for constructing and evaluating future PED systems. The goal of this work is to demonstrate that this method can make bulk structural electron crystallography reliable and fast, with the vision that PED may in the near future become a reliable, versatile and ultimately routine tool for determining atomic structures.

1.1. The Electron Microscope in Crystallography

Historically, X-ray techniques have been at the forefront of structural crystallography owing to the development of probabilistic phasing algorithms in the 1950s, collectively called direct methods (DM), that overcame the crystallographic phase problem (Hauptman 1991). These techniques enabled recovery of the critical phase portion of the Fourier components that describe the structure, enabling straightforward determination of structure models from diffraction intensity measurements. While highly suitable for many types of materials studies, evidenced by the vast number of atomic structures elucidated using X-ray radiation over the past 50 years, high-resolution X-ray techniques have some disadvantages from the perspective of nanomaterials characterization:

- Laboratory X-ray sources are not bright enough for studying very thin crystals, surfaces, and interfaces. To obtain scattered intensities with large dynamic range, a bright source such as a synchrotron is necessary.
- The beam diameter from high brightness sources are on the order of 1 μm, and on the order of 0.5 μm in specialized fine-probe laboratory instruments (an exception is the use of Fresnel zone plates that can obtain 100 nm probes in synchrotrons (Suzuki et al. 2005), however they are extremely rare due to cost). In particular:
  - Single crystal dimensions generally must be on the order of the probe size. Heterogeneous materials cannot be studied unless crystallites are larger in size or can be isolated.
  - Nanocrystal studies require powder specimens or homogeneous polycrystals, which generate ring patterns from simultaneous sampling of all orientations of the crystal. Symmetry information is lost in ring patterns and must be acquired using other techniques such as transmission electron diffraction (TED). Additionally, because reflection number scales roughly with the cube of spatial frequency, large cell structures will have overwhelming peak overlap.
  - Peak resolution (line width) is limited by the width of the probe. Decreasing the probe size can cause ring overlap in dense diffraction patterns from large cell materials or superstructures.
- X-ray imaging optics with adequate resolution are not available; the only information from experiments are diffraction intensities. Morphological and defect information is thus not simultaneously available.

- Being a shared resource, synchrotron-based research projects have strict time constraints and shared maintenance costs.

TEM has traditionally played a complementary role to X-ray methods in crystallography, partly because image resolution was insufficient except in specialized high-energy instruments and also because data quality from TED was limited by multiple scattering. Nevertheless, the ability to form a fine probe and to simultaneously collect diffraction patterns are distinct advantages. In recent years, the field has seen a huge leap in the imaging capabilities of high-resolution imaging (HREM) and scanning modes (STEM) due to the introduction of aberration-corrective optics allowing point resolutions of less than 1 Ångstrøm (Haider et al. 1998; Batson et al. 2002; Haider et al. 1999; Nellist et al. 2004). Unfortunately, atomic resolution images are beyond the reach of most researchers because aberration correctors are still extremely expensive; the vast majority of TEMs are still limited by the resolution of the image-forming optics.

Electron diffraction is a complementary technique that is capable of extracting structural information — albeit incomplete because phase is lost — to much higher resolution (sub-picometer regime) than imaging techniques because it is virtually immune to the resolution-limiting aberrations of the objective lens. It can often be combined with imaging to enhance the resolution of HREM images through the phase extension technique. A probe size of under 25 nm is readily achieved on modern instruments, enabling precise study of very small particles, individual crystallites within a heterogeneous matrix, and fine structures such as interfaces and surfaces in the TEM. This resolves a major constraint posed by X-ray methods.

While the combination of imaging and diffraction tools is very powerful, a central theme in this thesis will be rapid structural characterization. For raw speed, diffraction alone is an ideal technique. Immunity to aberrations in the image-forming optics allows information transfer to extremely high resolution (≈ 0.01 Å), circumventing the need for careful alignments or in the extreme case aberration-corrective optics. Because it is an averaging technique, it is insensitive to instabilities such as instrument vibration, and the effect of non-periodic features such as defects are diminished (this can be a disadvantage depending on the information sought). Additionally, structural information is collected within highly localized features in the form of diffraction spots or Kikuchi lines; consequently, low dose is possible because the signal to noise ratio is high, minimizing radiation damage to the specimen. This is especially critical for structures that damage easily such as open-framework structures and biological molecules.

Electron diffraction has seen limited use as a standalone structural crystallography technique due to problems of data quality arising from multiple scattering, discussed later in section 1.3. This is rapidly changing, as methods are now available (section 1.4) to improve the quality of the data or take advantage of cases where data are kinematical or near-kinematical for effective use with DM. As will be seen in the next section, DM is very robust provided that data quality is sufficient.

1.2. Direct Methods

A structure projection in two dimensions can be represented by a two-dimensional function $f(\mathbf{r})$, where $\mathbf{r} = x\mathbf{a} + y\mathbf{b}$. Diffraction experiments yield information about this function through the Fourier transform relationships:

$$(1.1) \qquad f(\mathbf{r}) = \int_{-\infty}^{\infty} F(\mathbf{k})e^{2\pi i\mathbf{k}.\mathbf{r}}dk$$

$$(1.2) \qquad F(\mathbf{k}) = \int_{-\infty}^{\infty} f(\mathbf{r})e^{-2\pi i\mathbf{k}.\mathbf{r}}dr,$$

where $\mathbf{k} = h\mathbf{a}^* + k\mathbf{b}^*$ and $\mathbf{a}^*$ and $\mathbf{b}^*$ are unit vectors in reciprocal space. It should be noted that this is a crystallographic structure projection so $\mathbf{a}$ and $\mathbf{b}$ are direct lattice vectors, and additionally $f(\mathbf{r})$ is a potential since in electron diffraction the incident beam interacts with the electrostatic potential. The Fourier transform of a periodic structure, $F(\mathbf{k})$, comprises discrete harmonic components (*structure factors*) that are described by an amplitude term $|F(\mathbf{g})|$ and complex phase term $e^{i\phi_g}$, where $\mathbf{g}$ is a reflection vector in reciprocal space. Assuming for the moment that dynamical multiple scattering can be ignored, the intensities measured in a diffraction pattern are related to the structure factor amplitude by $I(\mathbf{g}) = |F(\mathbf{g})|^2$, and the phases are lost. If phases were available, Fourier inversion via equation 1.1 would generate the structure $f(\mathbf{r})$. This is known as the phase problem of crystallography, and recovery of the phases is the central concept of direct methods.

Refinement procedures are very successful at pinpointing the structure to high accuracy given that the model structure from which the refinement is based is already close to the true structure (e.g. deviating by less than ≈ 0.2 Å) (Marks et al. 1998). The difficulty lies in the fact that, unless the set of initial models considered for refinement contains a close approximation to the true structure, the true structure will (almost without exception) never be found. The primary challenge in structure determination is therefore the generation of a small set of potential structures from which a refinement can be based, and which includes the true structure. It is of relevance to note that the phases are more important than the absolute values of the moduli that are measured. That is, the component providing the key spatial information in a structure is the phase. This is advantageous since the problem is rather forgiving from a probabilistic standpoint: the intensities can vary by a large amount but as long as the recovered phases are close to true values the structure is still inherently recognizable, and even the phases can deviate by a small amount without losing interpretability (figure 1.1).

In simple terms, direct methods make use of *a priori* information to constrain the phases of measured reflections. DM codes exploit this information to converge rapidly to a small set of possible solutions, which usually contains the true solution provided that the intensity data are of sufficient quality. Some of the common constraints used are:
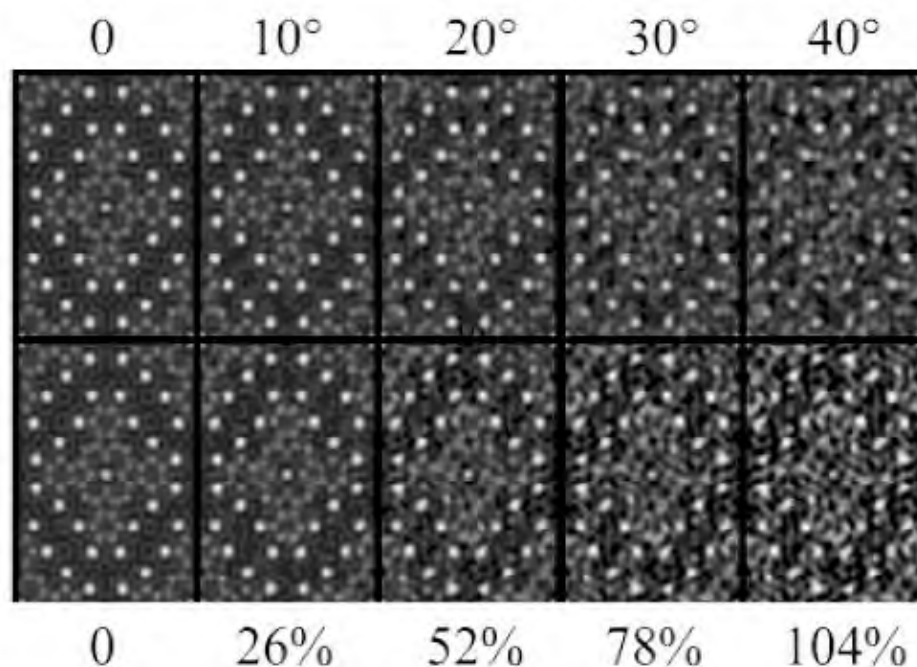
Figure 1.1.   Demonstration of amplitude and phase errors in perbromo-phthalocyanine. The bottom row shows amplitude errors (a modified R_1 - see eqn 1.17) and the top shows phase errors (standard deviations, columns give comparable R-factor), both increasing to the right. Amplitude errors were generated using noise in steps of 8% of the strongest beam amplitude. Reproduced from Marks and Sinkler (2003).

(1) Atomicity: Scattering originates from atoms and hence the solution should have atomic features; regions of peak-like charge densities correspond approximately to isolated atom charge densities.

(2) Cell density: Assuming the data has ample resolution (≈ 1 Å), most of the charge density in the unit cell is zero, representing the space between the atoms.

(3) Positivity: Charge density in a real crystal is always positive.

(4) Localization: If solving a structure in three dimensions, atoms will only be displaced from bulk positions in a narrow region at the surface.

Two major families of algorithms are currently used: 1) approaches based upon probability relationships existing between amplitude and phase, and 2) approaches using iterative mathematical projections. Probabilistic approaches were pioneered in the 1950s and have been very popular in X-ray crystallography, while projection methods are a more general case that have proven to be versatile and robust.

1.2.1. Probabilistic Direct Methods

The structure factor is defined in terms of the unit cell contents as:

$$(1.3) \qquad F(\mathbf{g}) = \sum_{i=1}^{N} f_i e^{2\pi i \mathbf{g}.r_i},$$

where N is the number of atoms in the unit cell and f_i is the scattering factor for the ith atom in the unit cell. It is convenient in direct methods to normalize the structure factors to the largest value the amplitude can take on as defined by the unit cell contents, resulting in *unitary structure factors* defined by,

$$(1.4) \qquad U(\mathbf{g}) = \sum_{i=1}^{N} \left(f_i / \sum_{j=1}^{N} f_j \right) e^{2\pi i \mathbf{g}.r_i} = \sum_{i=1}^{N} n_i e^{2\pi i \mathbf{g}.r_i},$$

where n_i is the unitary scattering factor. Many direct methods flavors make use of a more complicated normalization, denoted $E_{\mathbf{g}}$, that generates similar results to the relationships derived below. To obtain E's, the structure factor is simply divided by the sum of the scattering factors.

Harker and Kasper were the first to show that structure factor amplitudes could give information about structure factor phases (Harker and Kasper 1948). Using Cauchy's inequality, they proved that for a centrosymmetric crystal (one with an inversion center), all structure factors are forced to be real and phase determination becomes a sign determination problem according to the relationship:

$$(1.5) \qquad U^2(\mathbf{g}) \leq \frac{1}{2} \left[1 + U(2\mathbf{g}) \right].$$

If $U^2(\mathbf{g}) > \frac{1}{2}$ then $U(2\mathbf{g}) \geq 0$, or in other words the sign of reflection $U(2\mathbf{g})$ is positive regardless of the value of $|U(2\mathbf{g})|$. This inequality opened the field of direct methods.

The primary breakthrough in direct methods was the development of the triplet formulation which allows phase determination of a given reflection by two others that are related statistically. This is used in the majority of direct methods algorithms. The earliest form of this is the Sayre equation, derived from Fourier theory using a simple convolution:

$$(1.6) \qquad F_{\mathbf{g}} = \frac{\theta_{\mathbf{g}}}{V} \sum_{\mathbf{h}} F_{\mathbf{h}} F_{\mathbf{g}-\mathbf{h}},$$

where $\theta_{\mathbf{g}}$ is the ratio of the atomic form factor to the squared atomic form factor and V is the unit cell volume (Sayre 1952) (subscripts will be used as a shorthand to indicate the quantity corresponds to the given reflection denoted by the subscript). This relationship takes advantage of atomicity: if $f(\mathbf{r})$ is squared then atomic features become more sharply defined

but the positions remain the same and accordingly the phases for the structure factors are the same. Rewriting this we get,

$$(1.7) \qquad |F_{\mathbf{g}}|e^{i\phi_{\mathbf{g}}} = \frac{\theta_{\mathbf{g}}}{V} \sum_{\mathbf{h}} |F_{\mathbf{h}}F_{\mathbf{g}-\mathbf{h}}|e^{i(\phi_{\mathbf{h}}+\phi_{\mathbf{g}-\mathbf{h}})},$$

hence,

$$(1.8) \qquad \phi_{\mathbf{g}} \approx \phi_{\mathbf{h}} + \phi_{\mathbf{g}-\mathbf{h}}.$$

Rearranging gives the triplet relation for the phases:

$$(1.9) \qquad \phi_{-\mathbf{g}} + \phi_{\mathbf{h}} + \phi_{\mathbf{g}-\mathbf{h}} \approx 2n\pi,$$

where n is an integer. The relationship is illustrated by the Argand diagram in figure 1.2 for a five-term summation for the right hand side of equation 1.7. If the magnitude $|F_{\mathbf{g}}|$ of reflection $\mathbf{g}$ is large and $|F_{\mathbf{h}}|$ and $|F_{\mathbf{g}-\mathbf{h}}|$ are also large for a particular value $\mathbf{h} = \mathbf{h}'$, the sum becomes dominated by the $\mathbf{h}'$ term. The vector sums must match, and even though the phases for smaller terms may deviate, the phase of the component $F_{\mathbf{h}'}F_{(\mathbf{g}-\mathbf{h}')}$ approximates that of reflection $\mathbf{h}$. The probability distribution was derived by Cochran (Cochran 1955) demonstrating that equation 1.9 is statistically sound and that for strong reflections — which contribute strongly to structural features — it becomes distinctly peaked at $2n\pi$ phase difference.

Practical application of the triplet relation within direct methods begins by defining the phases for a small subset of the reflections in the intensity data set (called the basis set). These are preferably strong reflections for which the true phases may or may not be known; if unknown, random phases are usually given. By propagating triplet relationships in a process called phase extension, estimates of the phases of the remaining reflections can be determined. The phases are probabilistic, hence even if the starting phases are correct, the extended phases may not be correct though usually they are indeed correct or close. Additionally, the phase-extended solution must necessarily be self-consistent, e.g. for a given reflection of unknown phase, multiple reflection vector pairs can define its phase so it may receive conflicting phase assignments. In such a case it is necessary to eliminate discrepancies by modifying some of the starting phases. The key to finding probable starting structures is to rapidly search through solutions to find the ones that are self-consistent for all the measured reflections. A figure of merit (FOM) is calculated to measure the correctness of the potential solutions, and the solutions can be ranked based according to their FOMs. The solution with the lowest FOM is not necessarily the true solution, however the correct solution will necessarily have a low FOM.

1.2.2. Feasible Sets

Alternate methods based upon iterative projection methods were developed for analogous problems concerning information recovery in mathematics and signal processing. The fundamental
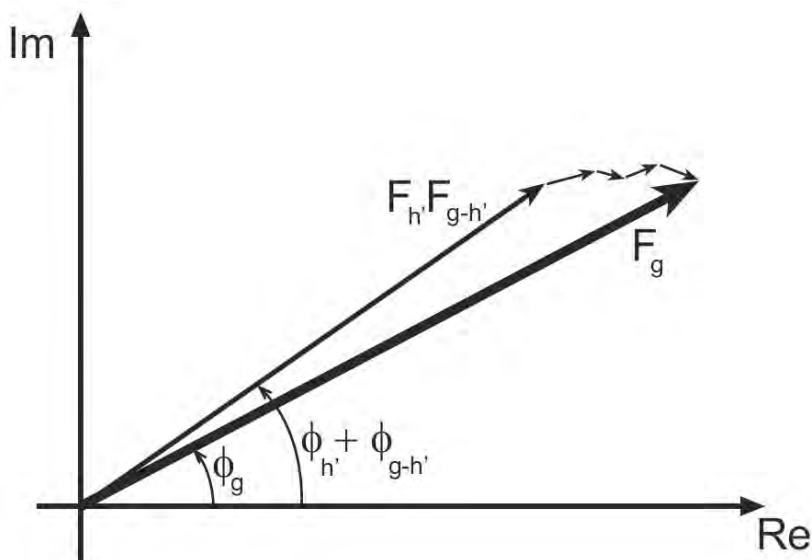
Figure 1.2.   Argand diagram illustrating Sayre's triplet relationship (equation 1.9). For strong amplitudes $|F_{\mathbf{g}}|$, $|F_{\mathbf{h}'}|$, and $|F_{\mathbf{g}-\mathbf{h}'}|$, the phase sum is approximately $2n\pi$.

idea is to group possible solutions into a *feasible set* and rapidly determine their overlap (potential solutions) through the use of projection operators. A set is a general term describing a group of entities that satisfies certain conditions and constraints. In the context of structural crystallography, two sets are of relevance: 1) the set S_1 of structure factors $|U_g^{exp}|e^{i\phi\mathbf{g}}$ that have been constrained by the experiment; and 2) the set S_2 that satisfies atomistic constraints, itself comprising the overlap of independent sets defined by the *a priori* constraints listed in the previous section. These sets are depicted graphically in fig 1.3. The projection operator is employed within an iterative sequence, and is described by the projection direction, for example,

$$(1.10) \qquad\qquad (U_{\mathbf{g}})_{n+1} = P_2 P_1 (U_{\mathbf{g}})_n.$$

In relation 1.10, P_1 is the projection from set S_1 to S_2 and P_2 is the projection from set S_2 back to S_1.

An important property of a set is convexity: a set is convex if it contains all points on a line connecting any two of its members. A strong convergence is observed if both sets are convex (Youla 1987). Unfortunately, the set S_1 constrained by experimental amplitudes exclusively is not convex (whereas the related set where phases are known, excluding moduli, is convex), so a strong convergence is not guaranteed. However, for the general case of non-convex sets it was shown that the iteration can at worst only stagnate (Levi and Stark 1984).

The problem space is uniquely defined by the constraints imposed upon the sets being explored. Depending upon the way these constraints are defined, three possible outcomes are
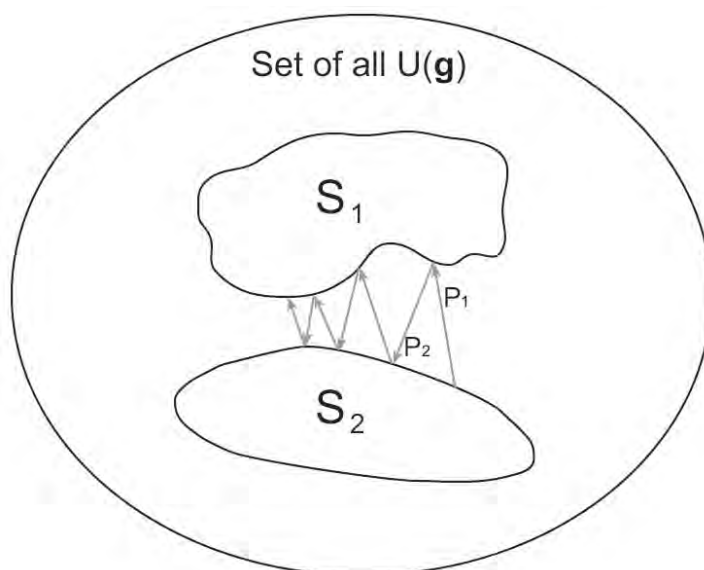
Figure 1.3. Graphical representation of iterative projection onto sets described by equation 1.10. S_1 is the set of structure factors constrained by the observed experimental intensities $|U_g^{exp}|e^{i\phi_{\mathbf{g}}}$ and S_2 is the set of structure factors that satisfies the *a priori* constraints. The magnitude of P_n represents the calculated figure of merit (FOM); rapid convergence toward a feasible solution accompanies minimization of the FOM.

possible (see figure 1.4). In an ideal case, a uniquely defined solution (figure 1.4(a)) is recovered that satisfies all constraints within the sets. This is almost never the case, and typically there is an intersection of sets or no intersection (figures 1.4(b) and (c), respectively). In the case where there is overlap, there may be a large number of potential solutions (Combettes 1996) and additional constraints can be imposed — for example a uniqueness constraint to filter out redundant "like" solutions — to reduce the number of feasible solutions. In the third case, where constraints are too strict, no overlap occurs and the projection algorithm attempts to decrease the distance between sets, in other words it will minimize the figure of merit as best it can. An example is the case where measured amplitudes deviate from kinematical too strongly, giving solutions that do not make chemical sense (e.g. the potential map indicates atoms that are too close). In defining the problem, the constraints are ideally balanced to minimize the number of potential solutions without overly constraining the feasible sets. A consequence of having a non-convex set is that all three cases can be simultaneously satisfied. More than one local minimum is available, and a feasible set of discontinuous solutions can be generated, i.e. multiple solution families with different defining features.

The various flavors of direct methods can be interpreted from the projection standpoint through the identification of their projection operators and constraints. Classical direct methods can be interpreted as the iterative procedure incorporating 1) projection of the phases
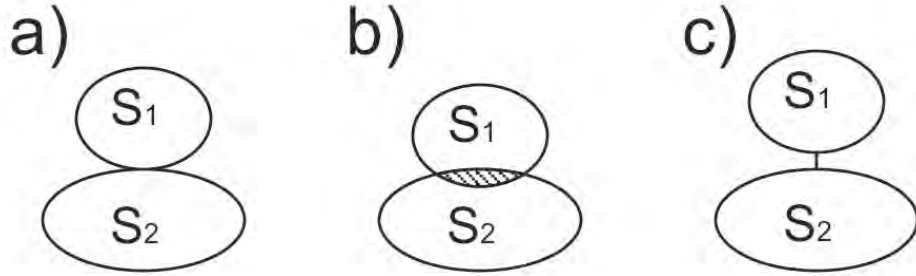
Figure 1.4. Three possible outcomes of the solution search between sets S_1 and S_2 using iterative projection. Case a), where a single unique solution is clearly defined, is rare. Case b) demonstrates considerable overlap of sets, a consequence of loose constraints where many solutions satisfy both constraint sets. c) shows a case where there is no overlap between sets. The algorithm will seek the solutions that minimize the distance between the sets.

using probabilistic relationships (triplets, quartets, etc.), and 2) correction of the moduli. The iterative procedure used in the feasible sets '98 (fs98) code written at Northwestern University is shown in figure 1.2.2, and uses the projection operators:

$$(1.11) \qquad P_1 u_{\mathbf{r}} = \begin{cases} 0 & \text{if } u_{\mathbf{r}} < 0 \\ u_{\mathbf{r}} \ln \frac{u_{\mathbf{r}}}{\langle u_{\mathbf{r}} \rangle} & \text{if } u_{\mathbf{r}} > 0 \end{cases}$$

$$(1.12) \qquad P_2 U_{\mathbf{g}} = |U_{\mathbf{g}}^{exp}| e^{2\pi i \phi_{\mathbf{g}}}.$$

P_1 is a peak-sharpening projector similar to Sayre's squaring operation which ensures atom-like features and only positive charge density. P_2 re-constrains the solution in reciprocal space by correcting the moduli to known (experimental) values.

The projection cycle is monitored by a recovery criterion, the figure of merit (FOM), which serves as a metric for the algorithm's effectiveness and can optionally be used to determine when the algorithm should cease. Several types of FOMs are available with varying characteristics designed to minimize certain types of error; the one used in fs98 is as follows:

$$(1.13) \qquad FOM = \sum_{g \neq 0} \frac{|(U_{\mathbf{g}})_{n+1} - \alpha(U_{\mathbf{g}})_n|}{(U_{\mathbf{g}})_{n+1}},$$

where α is chosen to minimize equation 1.13. In the case of a true solution with no measurement error, equation 1.13 will be zero.
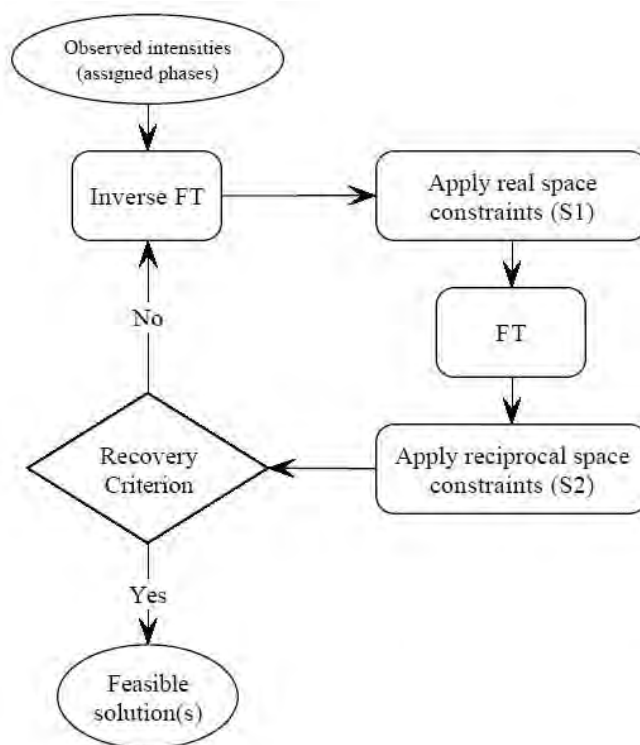
Figure 1.5. Flowchart of the feasible sets '98 (fs98) direct methods algorithm.

1.2.3. Genetic Algorithms

Due to the non-convexity of the amplitude constraint, the intersection of the crystallographic constraints could exist at any number of local minima. It is therefore important to probe all of these minima, as the true solution could be contained within any one of these intersections. Genetic algorithms are a powerful method to perform global search of the possible sets with low information overhead (Landree et al. 1997). They act similarly to the population growth of biological systems with environmental pressures, where offspring with enhanced adaptations are propagated with each successive generation.

In genetic algorithms, the starting phases of a basis set are defined as randomly chosen binary strings. The basis set is chosen based upon statistical relationships within the data set; in simple terms, strong reflections that define other beams are chosen with regard to potential phase relationships. This is done to avoid redundant solutions and to ensure convergence. About 10-20% of the total number of beams in the data set is included in the basis set. The binary string describing phases of the basis set is referred to as a chromosome. For example, each beam's phase — which in the centrosymmetric case can either be $0°$ or $180°$ — is represented by a single bit: 1 or 0. For each iterative projection the population is evaluated according to equation 1.13. After the individuals in an entire generation have been subjected to

iterative projection and evaluated by equation 1.13, a new generation is born through a process called cross-sharing. Here, the chromosome is broken up into schemata (short contiguous binary segments) which are randomly re-combined with schemata from other populations that have favorable FOM to generate new chromosomes to be used in the next iteration. The children generated with each iteration will generally have improved collective FOM due to natural selection.

To enhance the search capabilities, random mutations are introduced where a single bit or multiple bits within a chromosome are flipped. This causes new areas of solution space to be probed that would otherwise be missed due to non-convexity. Another enhancement, intended to prevent too rapid of convergence, is to sort schemata according to their similarity. This encourages parallel evolution of different 'species', effectively probing multiple niche solutions within the solution space. The algorithm with these enhancements tends to converge rapidly; in fs98 the algorithm is set to terminate by default after 36 populations.

In practical application, direct methods are very successful provided that the quality of intensities is sufficient. In the next section, it will be seen that in electron diffraction they usually are not (except in special cases) due to multiple scattering.

1.3. The Problem of Multiple Scattering

In the simplest interpretation, the radiation incident upon the specimen is scattered by the atomic planes of the crystal when the Bragg condition,

$$(1.14) \qquad \lambda = 2d \sin \theta_B,$$

is satisfied (d is the distance between scattering planes and θ_B is the Bragg angle). The ideal case for DM is when intensity in a diffracted beam is a result of single scattering events from the scattering planes (kinematical diffraction). For X-rays, the probability of scattering is already low, therefore the probability for multiple scattering is vanishingly small. The measured intensity is then related to structure factor according to the relationship,

$$(1.15) \qquad I_g^{exp} = |F_g|^2.$$

Electrons, however, interact more strongly with matter than X-rays by 3-4 orders of magnitude. The intensities of scattered beams deviate from kinematical and equation 1.15 no longer holds. This phenomenon, termed dynamical diffraction, is demonstrated in figure 1.6 for two beams. The probability for rediffraction is a function of specimen thickness, therefore as the electrons propagate through the specimen, intensity is continually exchanged between diffracted and transmitted beams. At the exit surface the diffracted beam intensity no longer represents the scattering strength as indicated by the structure factor.

In the configurations of high symmetry that are of most interest in crystallographic studies, many beams are simultaneously excited. Within a zone axis pattern (ZAP), a large number
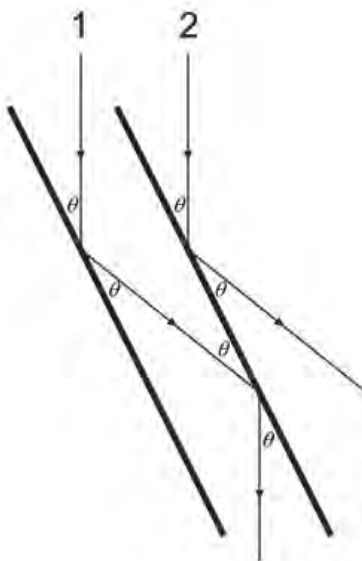
Figure 1.6. Diffracted beams that meet the Bragg condition (equation 1.14) are necessarily in the same condition to be rediffracted back into the incident beam. Demonstrated here for two beams, this is the origin of dynamical diffraction.

rediffraction paths are simultaneously available and the intensities in the pattern become distorted — more severely if strong scatterers (heavy elements) are present or if the specimen is thick. Images are likewise affected since the same beams contribute to the image: contrast oscillations of image features with increasing thickness prevent direct interpretation of HREM images except for suitably thin specimens. The quality of crystallographic information available in TEM is thus limited by the cell contents and their arrangement and by the specimen thickness. It is relevant for PED to note that much less intensity exchange occurs when only a few beams are simultaneously excited. If only two beams are strongly excited at a time, the least distortion of intensities occurs.

1.3.1. Multislice

In structure studies involving high resolution imaging, image simulation is used to account for the effects of multiple scattering. First, an image is simulated based upon a structure model, then it is checked to see how closely it resembles the experimental image, the structure is refined, and the process repeated. Like direct methods, many flavors of image simulation have been developed. The type employed in the analyses in the following chapters is the multislice approach.

Multislice describes the interaction of three components:

- ψ: The electron wave;

- P: The propagator of the electron wave in space;
- Q: A thin slice of the specimen projected onto a plane (phase grating).

The crystal is divided into N thin slices through which the electron wave propagates sequentially, where slice thickness $\times N$ is the specimen thickness. The multislice algorithm is described by the following general formula (Cowley and Moodie 1957):

$$(1.16) \qquad \psi_{n+1} = [\psi_n \cdot Q_n] \otimes P_{n \to n+1}.$$

The symbol $\otimes$ is the convolution operator. In a multislice routine, the incident beam is scattered by the phase grating (also called the transmission function, $e^{ik\phi}$) and the intensities of the diffracted beams are tracked. The potential within a slice n is iteratively projected using the propagator onto the next slice $n+1$ and the process is repeated until N total slices have been processed. The exit wavefunction is then collected and either used to form a diffraction pattern in reciprocal space or is convolved with the microscope function (contrast transfer function, any apertures, and environmental effects) to form a simulated image.

Multislice simulations are employed in some structure refinement procedures such as NUMIS and MSLS (Jansen et al. 1998). The starting structure determined by direct methods is used to calculate simulated patterns that are compared to the experimental intensities. A FOM is used to evaluate the goodness of fit, usually given as some error metric such as χ^2 or an R-factor as follows:

$$(1.17) \qquad R_1 = \frac{\sum_{\mathbf{g}} \left| F_g^{exp} - F_g^{calc} \right|}{\sum_{\mathbf{g}} \left| F_g^{exp} \right|};$$

$$(1.18) \qquad R_2 = \frac{\sum_{\mathbf{g}} \left| I_g^{exp} - I_g^{calc} \right|}{\sum_{\mathbf{g}} \left| I_g^{exp} \right|}.$$

During refinement, atom positions are relaxed iteratively and the simulation is repeated to minimize the error metric. The minimum R_1 is usually greater than 20% for electron diffraction data whereas it is usually less than 5-10% for X-ray data (compared to kinematical simulation), and sometimes less than 1% for some inorganics (e.g., Khattak et al. (1975); Newsam (1988); Yu et al. (1995)). The R_2 metric is typically larger than R_1 and can in some cases better describe how well structure factor ratios are preserved within the data set.

Here it is relevant to mention the effect of specimen thickness variation on electron diffraction data. In image-based structure solution techniques, it is likely that the simulated image will match some band of the experimental image if the simulated thickness is within the range of experimental thickness. While diffraction has much better signal-to-noise than

HREM, the experimental data does not often match simulation closely regardless of whether average experimental thickness is consistent with simulated thickness. This is because thickness and orientation variation affects all of the beams in the pattern; therefore one cannot readily differentiate the contributions to intensity from different thicknesses.

1.3.2. Dynamical Direct Methods

Simulation always requires an initial model. It is the role of direct methods to provide this. However, dynamical effects will affect the reliability of direct methods, especially for bulk structures, hence *a priori* knowledge about how dynamical data affects direct methods solutions is needed for proper interpretation of direct methods results. The structure map that is restored for moderately thin specimens (< 20 nm) closely resembles the modulus of the Babinet $|1-\psi(\mathbf{r})|$, where $\psi(\mathbf{r})$ is the complex exit wave (Sinkler et al. 1998a). Electron diffraction data can be expected to give structure maps with atom-like features for specimens up to moderate thickness, however they will be distorted with increasing thickness. It is therefore necessary to be conservative with their interpretation (Marks et al. 1998):

(1) Not all peaks will be in correct places, and often will be off by more than 10 pm;
(2) Charge density will not be correct;
(3) There may be too few or too many peaks.

Here, it is important to mention a special dynamical case of scattering dominated by a single atom type (Sinkler and Marks 1999a; Marks and Sinkler 2003). In the case of structures that project well, a channeling model is applicable that describes the shape of periodic oscillation of the electron wavefunction as it propagates down individual atomic columns. Mathematically, the shape of each atom in projection can be described by some two-dimensional complex function $a(\mathbf{r})$. By convolution, this yields the reciprocal space function,

$$(1.19) \qquad \Psi(\mathbf{k}) = A(\mathbf{k}) \sum_i e^{2\pi i \mathbf{k}.r_i},$$

where i represents the set of atom positions in projection and $A(\mathbf{k})$ is the complex atom shape function in reciprocal space. Hence,

$$(1.20) \qquad I(\mathbf{k}) = |A(\mathbf{k})|^2 \left| \sum_l e^{2\pi i \mathbf{k}.r_i} \right|^2$$

The amplitude term $A(\mathbf{k})$ can be replaced by any real function $B(\mathbf{k})$ that generates a real feature in the object plane. For example, one could use a function $B(\mathbf{k}) = S(\mathbf{k})|A(\mathbf{k})|$, where $S(\mathbf{k}) = \pm 1$. In this case, we have an effective atom in real space described by the real symmetric function $b(\mathbf{r})$. The important point is that there need not be a direct relationship between the true complex wavefunction and the recovered pseudoatom; the features simply have to be similar (e.g., satisfying an atomicity constraint). This is the origin of the correspondence between the

modulus of the Babinet and direct methods solutions: there needs not be a direct correlation between the two. In the special case where channeling conditions give rise to atom features of the same type (excluding other types), such as for the thickness range of 5-20 nm in GITO crystals, all positions of that type will be recovered by Direct Methods (Sinkler et al. 1998b).

It is clear that kinematical diffraction is a poor model for absolute electron diffraction intensities, yet, as seen above and in other cases, classical direct methods applied to manifestly dynamical data often works, although results are hard to predict (Sinkler et al. 1998a; Weirich 2004; Nicolopoulos et al. 1995; Dorset et al. 1997). For example, a light atom column may be recovered while a column of heavy atoms may be missing from the solutions. This is rather counterintuitive, however, the link between the two can be found by examining the statistics of dynamical scattering within the 1s channeling model (Hu et al. 2000; Chukhovskii et al. 2001). The important points are given below:

(1) Phases of $+\mathbf{g}$ and $-\mathbf{g}$ reflections obey, statistically, the relationship

$$(1.21) \qquad\qquad\qquad \phi_{\mathbf{g}} + \phi_{-\mathbf{g}} \approx 2n\pi + \alpha,$$

where α is a phase deviation constant. It is dependent upon the type of atoms present and the thickness, and not upon $\mathbf{g}$. When relationship 1.21 holds, the data represents an effective kinematical approximation to the true structure. This behavior is shown in figure 1.7(a)-(b) for thin crystals of $C_{32}Cl_{16}CuN_8$, reproduced from Hu et al. (2000).

(2) The triplet sum phases obey a similar relationship:

$$(1.22) \qquad\qquad\qquad \phi_{-\mathbf{g}} + \phi_{-\mathbf{g}} + \phi_{\mathbf{g}-\mathbf{h}} \approx 2n\pi + \beta,$$

where β is a deviation constant similar to α, also dependent upon the cell contents and specimen thickness. Figure 1.7(c)-(d) demonstrates this relationship, reproduced from Chukhovskii et al. (2001).

(3) Friedel's law — that intensity of symmetry equivalents must be equal — is not stricly obeyed in dynamical scattering, however, it is obeyed statistically (figure 1.8).

The key result is that the structure must project well and the thickness must be sufficiently small for direct methods to work on dynamical data. In the case of psuedo-kinematical dynamical data, α in the Friedel pair relationship and β within the triplet sum is close to zero, approximating the kinematical statistics. On the other hand, in dynamical direct methods, α and β can span any value between 0 and $2n\pi$. A caveat is that multiple atom features may cause the value of β to lose statistical significance, e.g., the statistics begin to break down when many types of atom features are present (poor projection) or when thickness is too large for direct methods to recover from the intensities phases that follow equation 1.22.

While dynamical direct methods has been seen to be quite effective in model systems, in addition to small thickness usually some prior knowledge of the unit cell is required to predict favorable conditions (such as emphasis of like atom types due to channeling). Because *ab*
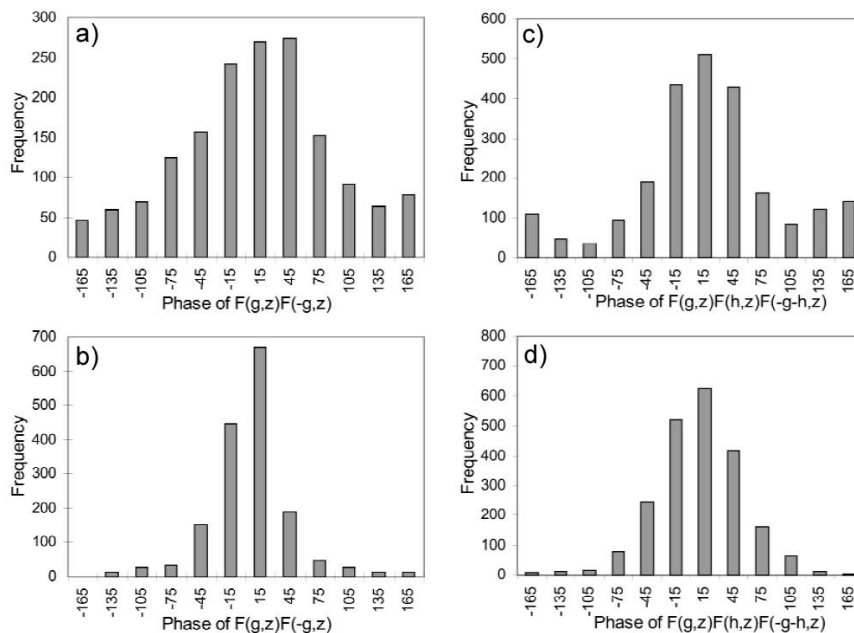
Figure 1.7. Probability histogram of the product $F_{\mathbf{g}}F_{-\mathbf{g}}$ for (a) centrosymmetric and (b) noncentrosymmetric (random) models of $C_{32}Cl_{16}CuN_8$ crystal. (c) and (d) are similar centrosymmetric and noncentrosymmetric histograms for the triple product $F_{\mathbf{g}}F_{\mathbf{h}}F_{-\mathbf{g}-\mathbf{h}}$ for the same crystal. All structure factors calculated by multislice, $t = 5.264$ nm. Taken from Hu et al. (2000) and Chukhovskii et al. (2001).

initio direct methods on TED data sets generally break down severely with increasing crystal thickness, it is difficult when working with novel systems to avoid pitfalls where not all atoms are simultaneously expressed, or where atom positions deviate too much to be usable as starting positions. For this reason, direct electron crystallography of novel complex bulk structures using conventional ED is still relatively impractical unless extremely thin and flat specimens are available. In spite of this, a small number of cases exist where data quality can be improved through clever means, of which PED is one form.

1.4. Approaches for Pseudo-Kinematical Electron Diffraction

As seen in section 1.2, if intensities are kinematical the structure factor phases are recoverable and the true structure easily retrieved. The method has been shown to be robust: intensities can vary by 10% or 20% in many situations and the phasing algorithm can still recover enough accurate phases to reconstruct the true structure or something very close. Apart from very simple structures such as silicon or magnesium oxide that are trivially solved by direct methods, there are a number of cases where electron diffraction data can yield starting structures suitable for refinement (Marks and Sinkler 2003). The most obvious case is that of
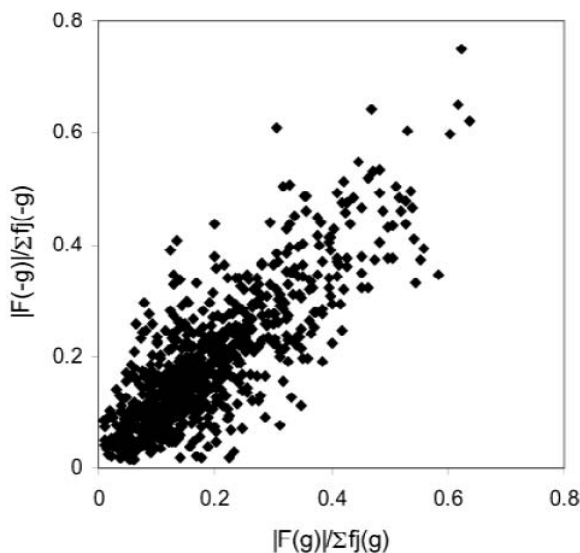
Figure 1.8. Normalized dynamical moduli of $F_{\mathbf{g}}$ plotted against $F_{-\mathbf{g}}$ for the noncentrosymmetric structure in figure 1.7(b) and (d). Friedel's law is obeyed statistically for this thickness (5.264nm).

thin specimens, however thickness must generally be on the order of 5-10 nm, or even less if the specimen contains heavy elements. This is difficult to achieve practically for many materials, and is also difficult for crushed (powder) specimens unless a definite cleavage plane for the zone of interest is present.

The logical extension of thin specimens is the case of surfaces, for which the Marks research group has considerable expertise. Special measures must be taken during the experiment, because a) substrate bulk spots are much stronger than surface spots and b) bulk spots necessarily overlap some surface spots in epitaxial superstructures and usually overlap for surface reconstructions, meaning in either case there are holes in the intensity data. The latter is addressed by an intensity prediction algorithm: rather than forcing unknown intensities to zero, therefore applying an incorrect constraint, an approach is taken that maximizes the entropy of the intensity summed over the real space map, in essence interpolating unknown reflections (Marks et al. 1998). Taking advantage of highly elongated reciprocal lattice rods arising from the Fourier transform along the surface normal, the measurement of surface reflections is made by tilting the substrate off the zone axis to damp multiple scattering by the bulk and to increase signal of surface reflections. The intensities measured by this technique are very close to kinematical and it is fairly straightforward to recover a good structure map.

A different class of approaches *assumes* deviation from kinematical. Instead of seeking kinematical data, it exploits the fact that the statistical relationships contained within the data set that code for phases (e.g., equation 1.6) may be preserved as long as relationships between

the intensity values are preserved (Marks and Sinkler 2003). This is called intensity mapping and requires that dynamical intensity relationships be consistent with kinematical:

$$(1.23) \qquad I_{\mathbf{g}} > I_{\mathbf{h}} \quad iff \quad |F_{\mathbf{g}}| > |F_{\mathbf{h}}|.$$

This interpretation is applicable to texture and powder patterns which provide an intensity averaging effect. The scattering from powder specimens has been described by Blackman (1939):

$$(1.24) \qquad \frac{I_{\mathbf{g}}^{dyn}}{I_{\mathbf{g}}^{kin}} = \frac{1}{A_{\mathbf{g}}} \int_0^{A_{\mathbf{g}}} J_0(2x)dx,$$

where $A_{\mathbf{g}}$ is an integration limit proportional to kinematical structure factor $F_{\mathbf{g}}$ and crystal thickness t. The ratio of any two reflections within a powder data set is thus given by:

$$(1.25) \qquad \frac{I_{\mathbf{g}}^{dyn}}{I_{\mathbf{h}}^{dyn}} = \frac{I_{\mathbf{g}}^{kin} F_{\mathbf{h}} \int_0^{A_{\mathbf{g}}} J_0(2x)dx}{I_{\mathbf{h}}^{kin} F_{\mathbf{g}} \int_0^{A_{\mathbf{h}}} J_0(2x)dx}.$$

The limits of equation 1.25 have interesting consequences. In the case of small A_g and A_h, the thickness and/or structure factor are small. The integral scales directly with A_g for small A, and equation 1.25 reduces to:

$$(1.26) \qquad \frac{I_{\mathbf{g}}^{dyn}}{I_{\mathbf{h}}^{dyn}} = \frac{I_{\mathbf{g}}^{kin}}{I_{\mathbf{h}}^{kin}}.$$

In the alternate case where A's are large, both integrals go to 1/2, and

$$(1.27) \qquad \frac{I_{\mathbf{g}}^{dyn}}{I_{\mathbf{h}}^{dyn}} = \frac{F_{\mathbf{g}}^{kin}}{F_{\mathbf{h}}^{kin}}.$$

In the worst case corresponding to the first two zeros of the Bessel function where $A_g \approx 1.2$ and $A_h \approx 2.75$ (see figure 1.9),

$$(1.28) \qquad \frac{I_{\mathbf{g}}^{dyn}}{I_{\mathbf{h}}^{dyn}} \approx 0.454 \frac{F_{\mathbf{g}}}{F_{\mathbf{h}}} \approx 1.$$

The order is still preserved, consistent with equation 1.23, implying that the statistical relationships generated by this ordering will also be preserved. This has been supported in experimental work by Vainshtein and also by Dorset (Vainshtein 1964; Vainshtein et al. 1992; Dorset 1995). The Blackman formula will be revisited in significant detail in chapter 4.
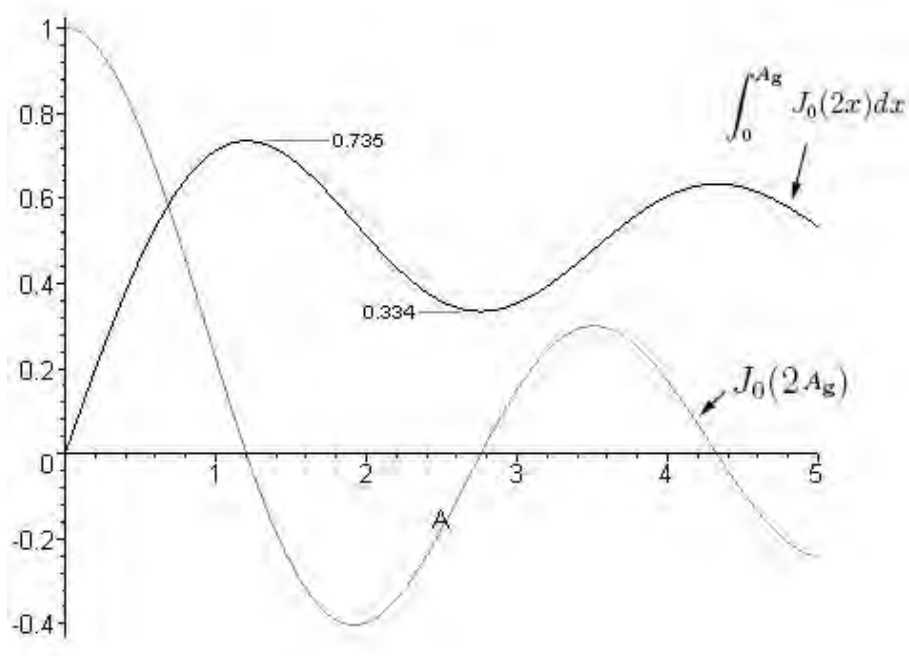
Figure 1.9.   Plot of the $J_0(2A)$ and its integral.   Values for the first local maximum and minimum are indicated.

1.4.1. The Precession Technique

Intensities in lamellar texture patterns and powder patterns demonstrate a clear relationship with structure factor as seen in equation 1.24, and the role of thickness has been characterized relatively simply. These intensities represent a statistical integration of off-axis conditions where dynamical coupling between many beams is minimized. In the case of texture patterns, a limited window of off-axis conditions is sampled whereas for powder patterns, all off-axis conditions are sampled. In large-angle convergent beam electron diffraction (CBED) studies, the same effect has been noted for high order Laue zone (HOLZ) reflections (Vincent et al. 1984; Vincent and Bird 1986). In the condition that the convergence angle is increased to the radius of the first order Laue zone (FOLZ), the high order reflections become filled with bright excess lines that map the Bragg condition for those reflections. The intensities of the lines were found to be two-beam in character and became kinematic in small crystals, fitting the Blackman description (equation 1.24).

Integration of k-line segments is difficult from a measurement standpoint. The precession electron diffraction (PED) mode stemmed from this work, devised as a method to facilitate easier measurement of the HOLZ reflections (Vincent and Midgley 1994). The unforeseen advantage, however, was that not only did precession integrate HOLZ reflections, the rest of the zone axis pattern became available for measurement with similar expected improvements

in data quality. Because it was devised with both data quality and measurement simplicity in mind, it is especially promising as a method for obtaining psuedo-kinematical datasets.

In the experimental configuration for electron beam precession, the incident illumination (can be convergent or parallel) is tilted off zone to large angle ϕ — typically 25-50 mrad corresponding to a reciprocal resolution on the order of an inverse Ångstrøm at 200 kV — and precessed in a serial manner about the optic axis forming an effective hollow cone of illumination upon the specimen (figure 1.10). The diffracted intensities, which constitute an off-zone diffraction experiment for each individual tilt, are de-scanned in a complementary manner to the tilt scan signal restoring the spots to their default zone axis pattern locations. This results in an effective integration of all tilts within the hollow illumination cone, i.e., around the edge of the cone. The PED pattern is thus an interpretable ZAP containing integrated intensities from off-zone conditions that are by nature less dynamical because fewer beams are simultaneously excited: strongly excited beams have little opportunity to exchange intensity with others (except for the transmitted).

This geometry yields several very interesting features:

- The pattern may be indexed as a conventional diffraction pattern while the intensities have actually been gathered from off-zone reflection conditions.
- Inelastic dynamical effects such as Kikuchi lines and intensity variations in CBED spots are reduced by averaging over incident beam directions.
- Since the beam is entering the sample from an off-axis direction, much of the dynamical scattering that is particularly strong at the exact Bragg condition (or zone axis channeling condition) is avoided.
- Many more FOLZ reflections are excited, under more kinematical conditions, by the Ewald sphere allowing the acquisition of an increased number of intensities for use in structure solution techniques.
- More HOLZ reflections are illuminated, yielding expanded 3-dimensional data sets provided that spots from separate Laue zones do not overlap.

Figures 1.11(a)-(b) demonstrate these characteristics in the diffraction pattern from a thick magnesium orthovanadate ($Mg_3V_2O_8$) crystal. The precession pattern was captured in selected area precession mode on the Hitachi UHV H-9000 modified for precession (Appendix B). A very moderate precession angle ($\approx$ 5 mrad) was used to form the pattern in 1.11(b). The extension by precession of the HOLZ ring into an annulus of width $\approx$ 10 mrad is clearly seen, as well as blending of inelastic dynamical effects into a radially diffuse background. This dynamical background suppression can improve intensity measurements by considerably simplifying the problem of background subtraction.

The improved quality of the precession data over that of conventional ED has been demonstrated experimentally (Vincent and Midgley 1994; Own et al. 2004), and a small number of structures have been solved via the technique, some *a priori* (Gjønnes et al. 1998a; Gemmi et al. 2003; Own and Marks 2005b), and others by a combination of simulation and/or correction using forward calculations (Vincent and Midgley 1994; Gjønnes et al. 1998b). Additionally,
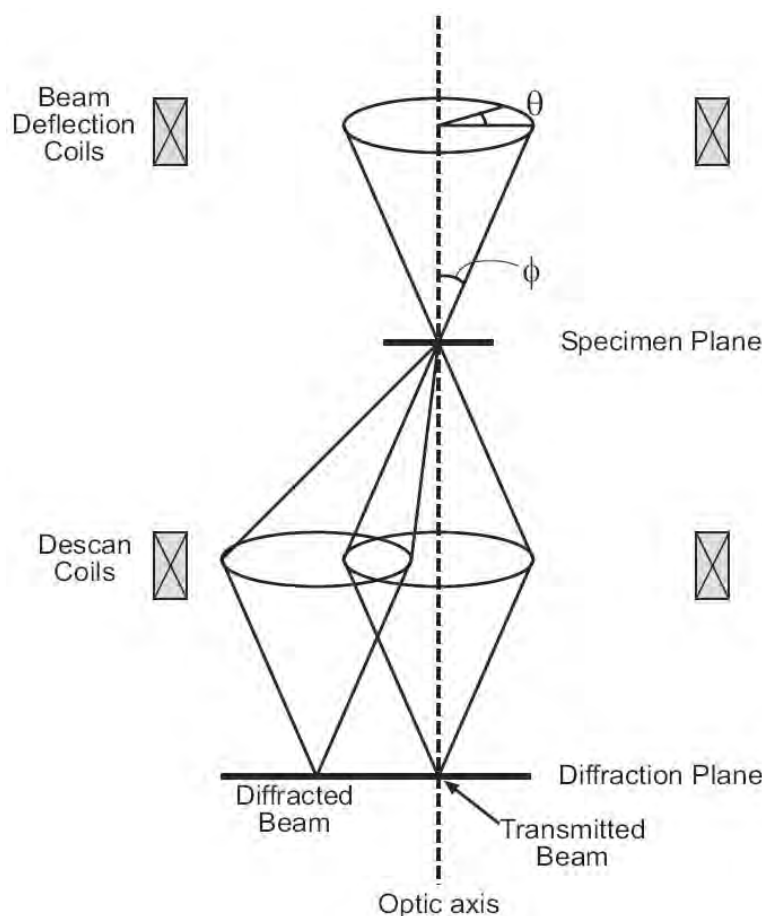
Figure 1.10. The schematic diagram of precession electron diffraction (PED). The beam is tilted off zone by angle ϕ using the beam tilt coils and serially precessed through an angle $\theta = 2\pi$. A complementary de-tilt is provided below the specimen by de-scan coils to restore the zone axis pattern.

precession has been used to derive Debye-Waller temperature factors from monatomic specimens using Wilson plots with good accuracy (Midgley et al. 1998). Some of the capabilities demonstrated by the technique are listed below:

(1) Pseudo-kinematical intensities are available under some experimental conditions as will be seen below;

(2) 3-dimensional datasets can be acquired under appropriate conditions from a single zone axis pattern. Low electron energy or large cell dimension in the optic axis are necessary, and Laue zone overlap must be avoided (see section 2.1);

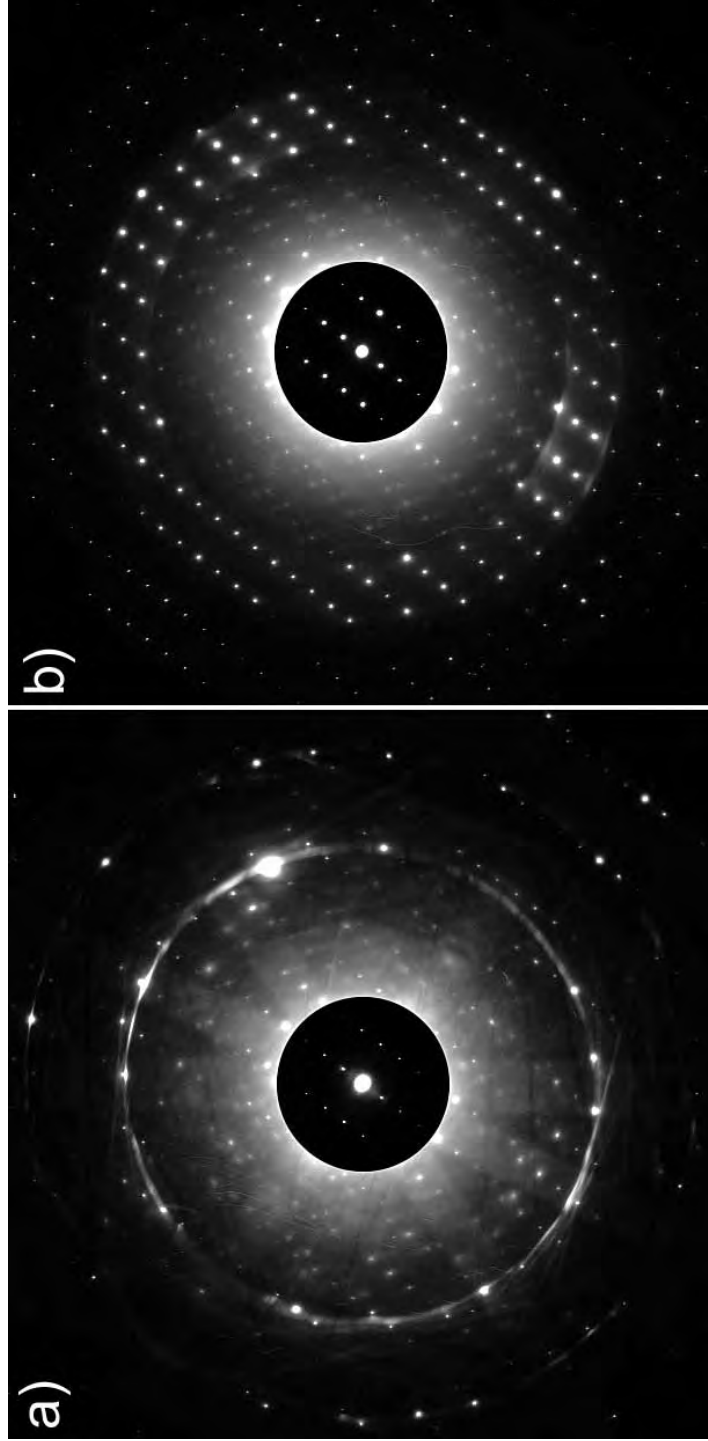(3) Decreased intensity oscillation with thickness is observed (also occurs with thickness averaging);

Figure 1.11. (a) Selected area DP of the [532] zone axis of magnesium orthovanadate ($Mg_3V_2O_8$). (b) Precessed SADP of the same orthovanadate using a moderate precession angle of 5.2 mrad to illustrate the effects. Several HOLZ annuli are apparent and non-systematic effects in the ZOLZ are averaged into a radially diminishing background. Note: Images (a) and (b) have identical exposure times, digitizing conditions, and have received the same digital image processing, so they can be directly compared.

(4) Greater tolerance to orientational errors, and specimens do not have to be perfectly on-zone to obtain symmetric patterns;

(5) Consistency of intensity values among different projections allows more accurate merging of multiple 2D projections into 3D datasets;

(6) Enhancement of fine detail in the solution of a large structure over that of conventional TED (Gemmi et al. 2003);

(7) If some structure factors are known, precession can be used to gain crystal thickness information with reasonable accuracy (within 10-15 nm).

1.4.2. Past Studies using PED

While promising, *a priori* structure determination of unknown or partially-known phases using PED has met with varied success, primarily because a rigorous understanding of errors has not been established. The technique was originally devised to complement CBED techniques, augmenting known structure factors measured through other means. From the standpoint of being a standalone technique, it is understood that precession data are distorted by dynamical effects necessitating careful treatment of data (Own et al. 2004), however the approaches toward data treatment have not been fully consistent in structure studies thus far. It has been suggested that thin specimens are preferred in order to circumvent the dynamical effects, though it was not known how thin. Nevertheless, to be a robust technique precession must be able to reliably handle unknown specimens exhibiting a variety of scattering strengths and physical geometries.

A correction factor has been presented in the literature in various forms to treat the nonlinearities at larger crystal thickness (Gjønnes 1997). It comprises two parts, a geometry part that corrects for integration geometry effects (Lorentz portion), and a two-beam part that corrects for thickness-dependent dynamical effects (Blackman portion). Starting from the Lorentz-modified Blackman formula

$$(1.29) \qquad I_g^{exp} \propto \frac{A_{\mathbf{g}}}{\left(1 - \left(\frac{\mathbf{g}}{2R_0}\right)\right)} \int_0^{A_{\mathbf{g}}} J_0(x)dx,$$

where R_0 is the radius of the zeroth order Laue zone (ZOLZ), the approximate kinematical intensity can be derived from the experimental intensity I_g^{exp} using the correction term:

$$(1.30) \qquad I_g^{kin} \propto I_g^{corr} = \left(\left(1 - \left(\frac{\mathbf{g}}{2R_0}\right)\right) \frac{A_{\mathbf{g}}}{\int_0^{A_{\mathbf{g}}} J_0(x)dx} \right) I_g^{exp},$$

applicable for convergent beam PED. The original form (Vincent and Midgley (1994), not shown) was refined to improve the Lorentz portion, and a new form was also derived to augment the convergent illumination version with a parallel illumination form (Gjønnes 1997). A detailed

analysis of correction factors and their validity will be given in chapter 4. Note that the argument of the integrand in equations 1.29 and 1.30 is different from the Blackman formula integrand (equation 1.24). The value of $A_{\mathbf{g}}$ used — critical for calculating accurate correction factors — is not clearly defined in the literature. This discrepancy will also be addressed in chapter 4.

The correction factor refined by Gjønnes for parallel illumination was used in an *a priori* investigation of Ti_2P. The structure was investigated by combining several 2D projections into a 3D dataset and inverting using SIR97 DM software (Gemmi et al. 2003). The assumption was made that intensities were proportional to structure factor in the limit of large thickness, hence intensities were corrected only for precession geometry (not two-beam effects) before merging the projections, and corrected intensities were used with direct methods rather than amplitudes. The three precession datasets were found to merge much better than selected area electron diffraction (SAED) projections ($R_{1,2} = 13\%$ and $R_{1,3} = 22\%$; subscripts denote the experimental datasets being compared), facilitated in part because severe streaking effects arising due to disorder were eliminated in the precession data. The precession solution had a higher final R-value (36%) than the solution from SAED (27.3%), however the structure maps from precession localized additional peaks that were suppressed in SAED, helping to explain why the superstructure arises.

The refined correction in equation 1.30 was also used in an elaborate *a priori* investigation of a thick crystal (Al_mFe, with nominal thickness 150 nm) that involved correction of dynamical intensities starting from a small accurate set of starting structure factors (Gjønnes et al. 1998b; Cheng et al. 1996). Careful CBED measurements and simulation were required to extract a starting set of (h00) and (hk0) systematic rows. The thickness of the crystal was evaluated by comparing experimental precession intensities to simulated precession intensities generated using equation 1.29. The specimen was reported to be very thick, at about 150nm.

The raw data was then scaled by the Lorentz-corrected two-beam intensity relationships (equations 1.25 and 1.29) using the known structure factors to acquire new 'effective' structure factors (U_g^{eff}). The two-beam portion of the corrections were simplified based upon the assumption that thickness averaging damps intensity oscillations for large A_g, resulting in an average value centered around the integral (see figure 1.9). This allowed a closed-form calculation using an exponentially-damped sinc function instead of requiring integration of the Bessel function J_0. These effective structure factors represent less accurate but nevertheless quasi-kinematic amplitudes that augment the known (h00) and (hk0) structure factors, completing the dataset.

Phase extension using triplets starting from the high confidence reflections ((h00) and (hh0) rows) revealed inconsistencies in signs for some strong reflections, and Bethe potentials (Bethe 1928) were used to correct for 3-beam interaction effects of 330, 530, and 860 beams that defined phases for many beams in the dataset. This resulted in four structure possibilities that were analyzed individually using dynamical n-beam Bloch wave calculations based upon Bethe-corrected structure factors respective to each possible set. The best match showed a

moderately successful correlation of intensities with the uncorrected experimental amplitudes ($R_1 \approx 32\%$), and R_2 was slightly higher at about 38%.

Solution was possible because accurate structure factors were available for strong beams, allowing separate treatment of errant beams in an n-beam refinement (to first order) beyond the expected two-beam case. Bloch wave simulation was required to distinguish which of the corrected structure factors were satisfactory, and confirmed that precession intensities are still subject to strong dynamical multi-beam coupling, at least for very thick specimens. While this study shows promise that structure solution with thick specimens is possible using precession, the fundamental problem is that considerable information must already be known about the structure in order to solve it. The above study represents a classic example of a bootstrap approach to structure solution via electron diffraction, which is both time and resource-consuming — not practically rapid or accurate enough to be competitive with X-ray methods on a wider scale.

A parallel effort on the same material system was undertaken by J. Gjønnes et al. (1998a) using precession intensities corrected only with the Lorentz factor (no two-beam correction). A merged data set was created from eight projections, and intensities with known phases from energy-filtered CBED measurements (Cheng et al. 1996) were added to augment it. Linear scaling of intensities during the merge yielded excessive error, therefore a non-linear least-squares procedure was used. The errors were still quite large, with a standard error of 36% for 13 reflections common to four datasets, therefore the data merge was noted by the authors as the most uncertain step in the study. Multiple 3D codes were used to phase the dataset — a simple Fourier synthesis, MICE, and QTAN — and a chemically reasonable structure model was obtained. Refinement using SHELXL97 showed a poor fit with the corrected experimental intensities ($R_1 = 42\%$), however the shifts to the refined positions were not large (< 25 pm). Large deviations from experimental structure factors were found in the refinement of the $hk0$ reflections, indicating that non-systematic dynamical scattering was indeed present.

Comparing this study to K. Gjønnes et al. (1998b), both studies found similar structure results for the [001] projection. The $hk0$ structure factors with full correction (two-beam and Lorentz) matched the high-confidence CBED structure factors more closely than the structure factors with only Lorentz correction. Seeing as the merged dataset quality was somewhat uncertain, the authors attributed much of the success of the latter study (the 3D study) to the forgiving nature of statistical direct methods. The specimen was estimated to be very thick (≈ 100 nm), and dynamical effects were considered to be the major source of error in the study. It will be seen in chapter 3 that in addition to specimen thickness (and variability), precession cone semi-angle ϕ is a key variable in the reduction of dynamical effects in the data. Unfortunately, neither study reported this experimental parameter in detail (Berg et al. (1998) reported ϕ in the range of 16-43 mrad); it is likely that thickness variability combined with inconsistent precession angle were the source of the inconsistency between projections.

The essential requirement for PED is that its intensities must demonstrate systematic behavior following equation 1.23. Some indication of the errors being systematic and slowly

varying has been implied in literature results; for example, Gjønnes et al. (1998b) implies insensitivity of the correction factor to thickness variation, and the present theory indicates that the results should be pseudo-kinematical owing to the many similarities with powder and texture intensities. These postulates require validation. The next chapter concerns development and implementation of a new generation of high performance precession system on which to conduct precession studies, and in the following chapters PED is investigated in detail with the goal of discovering systematic behaviors within measured intensities. It will be seen that the behaviors indeed satisfy the intensity mapping constraint in several cases and are predictable.